THE JOURNAL OF PHYSICAL CHEMISTRY B

Article

Cite This: J. Phys. Chem. B 2018, 122, 12087−12096

pubs.acs.org/JPCB

Quantitative Assessment of Thermodynamic Theory in Elucidating the Behavior of Water under Hydrophobic Confinement

Mohsen Ghasemi,[†] Saeed Miri Ramsheh,[‡] and Sumit Sharma*,[‡]

[†]Department of Mechanical Engineering, Ohio University, Athens, Ohio 45701, United States

[‡]Department of Chemical and Biomolecular Engineering, Ohio University, Athens, Ohio 45701, United States

Supporting Information

ABSTRACT: A macroscopic thermodynamics-based theory that can quantitatively describe the behavior of water confined between hydrophobic solutes has so far remained elusive. In this work, we progress toward this goal by comparing the predictions of macroscopic theory with the results from computer simulations. We have determined free energy profiles of water confined between two nanometer-sized surfaces of varying hydrophobicity using molecular simulations and have estimated thermodynamic properties such as contact angle, line tension, and size of the critical vapor tube from independent simulations. We show that the scaling of free energy barrier to evaporation is fairly well captured by the factor $(D/2 + \lambda/\Upsilon_{LV})^2$, where D is the confinement gap and λ/Υ_{LV} is the ratio of line-tension and liquid−vapor surface tension. The radius of the critical vapor tube necessary for nucleating evaporation scales by the factor $(D/2 + \lambda/\Upsilon_{LV})$. Exclusion of the line-tension term from thermodynamic theory leads to a qualitative disagreement between theoretical predictions and results from molecular simulations. We also demonstrate that macroscopic theory that includes the line-tension term is able to quantitatively match the entire free energy profile associated with the formation of a vapor-tube inside the confined region for conditions when the vapor state is the most stable state. The match is however only qualitatively correct for the conditions when the liquid state is more stable. Overall, the conclusion is that the inclusion of line-tension in macroscopic theory is necessary to describe the behavior of water under nanoscale confinement between two hydrophobic solutes.

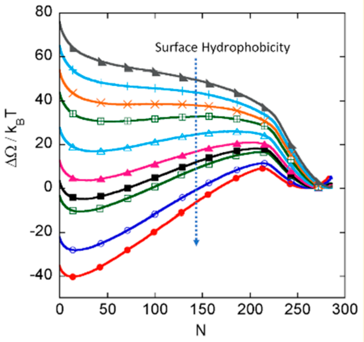

1. INTRODUCTION

Behavior of water in confined geometries has elicited much interest because of its important role in biological processes, such as protein−ligand[1,2] and protein−protein[3] association, folding of globular proteins,[4−6] formation of lipid vesicles,[7] operation of ion channels,[8] etc. Under ambient conditions, water forms a percolating, fluctuating network for hydrogen (H−) bonds. In the proximity of apolar solutes (solutes which are incapable of forming any H-bonds), the H-bond network of water gets disrupted. As a result, the behavior of water in such environments deviates significantly from the bulk. Near large apolar solutes (>1 nm), water exhibits enhanced density fluctuations akin to those at vapor−liquid interfaces.[9] If water is confined between two large apolar solutes, then below a critical confinement gap, d_c, the net unfavorable interactions of water with apolar solutes render the liquid state metastable with respect to the vapor.[10,11] As a consequence, water is expected to evaporate for confinement gaps below d_c. From thermodynamic considerations, the d_c of water confined between two macroscopic apolar solutes is of the order of micrometers (μm).[11] However, even for the confinement gaps less than d_c, water in the liquid state can persist in the confined region because evaporation requires overcoming an activation free energy barrier.[12,13] This free energy barrier is responsible for hysteresis that is observed between Cassie and Wenzel states in nanoscale grooved surfaces.[14,15] Evaporation of confined water proceeds via nucleation and growth of a critical vapor tube inside the confined region.[16,17] The activation barrier associated with formation of a critical vapor tube governs the kinetics of the evaporation process. Macroscopic thermodynamics-based expressions for free energy of formation of a vapor tube have been proposed[11,18] and modified to incorporate the role of line tension[13] and flexibility of confining solutes.[19] So far, most studies have shown a qualitative match between the thermodynamics-based free energy expressions and the free energy profiles of confined water obtained from molecular simulations insomuch that the thermodynamic quantities are treated as fitted parameters to the free energy profiles.[20] Interestingly, previous researchers have shown that the macroscopic capillary theory at liquid−vapor interface is quantitatively valid at length-scales as small as 2−10 nm.[21,22] The inclusion of line-tension in the expressions has remained contentious and its importance has not yet been carefully examined. In this work, we have performed molecular simulations to calculate the free energy profiles of water confined between two surfaces of varying hydrophobicity. Alongside, we have performed independent calculations of contact angle, line tension, and size of the

Received: September 14, 2018
Revised: November 21, 2018
Published: November 26, 2018

DOI: 10.1021/acs.jpcb.8b09026
J. Phys. Chem. B 2018, 122, 12087−12096

critical vapor tubes in confined water. We demonstrate that the inclusion of line-tension in macroscopic theory is essential for describing the scaling of the free energy barrier to evaporation; for matching the free energy profiles associated with the formation of a vapor tube in the confined region; and for the scaling of radius of the critical vapor tube. Since the ratio of line-tension and surface-tension is of molecular length-scales, the dependence on line-tension will be important when the confinement gap is of the order of nanometers. We show that the exclusion of line-tension from macroscopic theory leads to a qualitative mismatch between simulation results and theoretical predictions. We have also compared free energy profiles associated with the formation of vapor bubbles in the confined region with predictions from macroscopic theory. The macroscopic theory of vapor-bubble formation shows qualitatively correct trends for some range of surface hydrophobicity, but fails beyond this range. Therefore, the macroscopic theory of vapor-bubble formation needs to be reformulated.

2. SIMULATION SYSTEM AND METHODS

Figure 1 shows a snapshot of the simulation system. There are two hydrophobic surfaces submerged in water and placed parallel to each other. Each surface comprises of three layers of atoms arranged in a hexagonal lattice with a lattice constant of 1.4 Å mimicking a graphite layer.[16] The distance between the two adjacent layers of atoms in a surface is 2.5 Å. Confinement gap, D, is defined as the distance between the innermost layers of atoms of the two surfaces. D is kept fixed at 14 Å. Each layer is comprised of 550 atoms, so that each surface has a total of 1650 atoms. The lateral size of the surfaces is 30.099 × 29.503 Å^2 (∼30 × 30 Å^2 surfaces). Water molecules are modeled as simple point charge enhanced (SPC/E) (a rigid, three atom model of water).[23] The total number of water molecules in the simulation system is 11089. The approximate dimensions of the simulation box are 71.50 × 71.50 × 71.50 Å^3. The surface atoms interact with the oxygen atoms of water via Lennard-Jones (LJ) interactions with σ = 3.283 Å. The surfaces are treated as rigid bodies. For the outermost layer of atoms of the two surfaces, the oxygen-surface LJ well-depth parameter, ε is fixed at 0.0578 kcal/mol. To investigate the effect of surface hydrophobicity on the behavior of confined water, the ε of the inner two layers of atoms of the two surfaces is varied from 0.022 kcal/mol to 0.044 kcal/mol. Coulombic interactions are evaluated using Particle-Particle-Particle Mesh Ewald. In the isothermal−isobaric simulations (NPT ensemble), the temperature and pressure are fixed using the Nosé−Hoover thermostat and barostat, respectively.[24] The time-constant for the thermostat is fixed at 200 fs. The time-constant for the barostat is fixed at 2000 fs. A larger time-constant for barostat is employed because volume-change steps are computationally more expensive. The cutoff distance of Lennard-Jones interactions as well as the real-space part of the Ewald summation is taken as 9 Å.

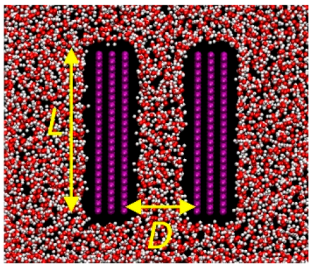

Figure 1. Snapshot of the simulation system. Two hydrophobic surfaces of lateral dimensions $L \times L$ are placed parallel to each other in water with the confinement gap D between them. Each hydrophobic surface comprising of three layers of atoms.

2.1. Indirect Umbrella Sampling (INDUS) Simulations.

In order to determine free energy profiles of water confined between the two surfaces, we employ indirect umbrella sampling (INDUS) methodology in molecular dynamics (MD) simulations in the isothermal−isobaric ensemble (constant temperature T, pressure P and number of particles N) with T = 300 K and P = 1 bar. INDUS[9,25] is a powerful technique to perform umbrella sampling in the reaction coordinate N within a MD simulation. Our implementation of INDUS methodology is similar to that of Remsing et. al,[20] wherein the confined region is defined as the probe volume. Within the probe volume a harmonic bias-potential based on N is applied, given by $U_{bias} = k(N - N_o)^2$, where k is the prefactor of the harmonic potential, N_o is set-point of the number of confined water molecules and N is the number of confined water molecules in any configuration. The above-specified bias-potential, which is commonly used in umbrella sampling simulations, will change discontinuously as molecules enter or exit the probe volume, which will lead to impulsive forces. To overcome this problem, in the INDUS approach, position of the particles is smeared in space by modeling their density by a continuous function centered at the particle.[25] This eliminates impulsive forces in the MD simulation. In the INDUS implementation, a Gaussian function is used for smearing the density. As a result, the bias-potential gets modified as $U_{bias} = k(\tilde{N} - \tilde{N}_o)^2$, where $\tilde{N}$ is the smeared-out number density of confined water.[25] By systematically varying $\tilde{N}_o$ from 0 to 280 in increments of 5, a set of overlapping umbrella sampling windows that span the entire range of densities inside the confined region are generated. In our simulations, we have chosen the truncation (or cutoff) length and standard deviation of the Gaussian function, r_c and s, to be 0.3 and 0.1 Å, respectively, to ensure a strong coupling between $\tilde{N}$ and N. The value of k is set to be 0.1 kcal/mol. Each INDUS simulation is done for 2 ns of equilibration followed by 8 ns of production run. Overall, 57 umbrella sampling windows are generated for each value of surface water interaction strength, ε. Free energy profiles as a function of N are generated using weighted histogram analysis method (WHAM).[26] The convergence of the free energy profiles is verified by doing additional 56 umbrella sampling simulations for surfaces with ε = 0.022, 0.0289, and 0.035 kcal/mol with $\tilde{N}_o$ set to 3, 8, 13,..283 and ensuring that the resulting free energy profiles with these additional simulations are indistinguishable from the previously obtained ones. Figure 2 shows a typical free energy profile that is obtained. Along with the free energy profile, Figure 2 shows snapshots of configurations at different stages in the free energy profile. At the local maximum, a vapor tube is formed in the confined region. This vapor tube grows in size and eventually, in the vapor basin, the entire confined region is devoid of liquid water.

2.2. Determination of Critical Radius of Vapor Tube.

Committer Analysis. We perform committer analysis for identifying configurations that comprise the transition state ensemble (TSE) for the transition from the liquid to the vapor state of confined water. The TSE is expected to be close to the

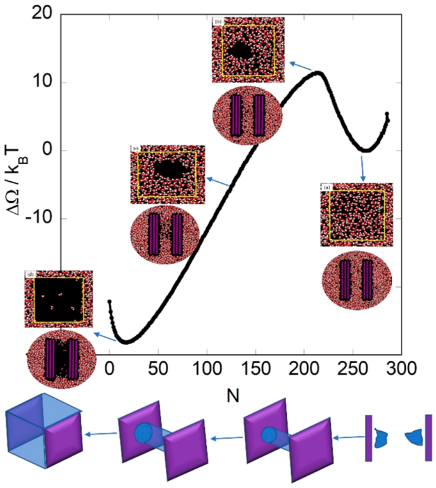

Figure 2. Typical free energy profile of water confined between two hydrophobic surfaces as a function of the number of confined water molecules, *N*. The free energy basin close to *N* = 10 is the vapor basin, and the one close to *N* = 270 is the liquid basin. Snapshots of configurations of confined water are shown at different stages. In the liquid basin, vapor bubbles form close to the hydrophobic surfaces. At the peak of the free energy profile, a vapor tube is clearly seen in the snapshot. For smaller values of *N*, the vapor tube grows in size. In the vapor basin, the entire confined region is devoid of water.

peak in the free energy profiles. Hence, we harvest 300−350 randomly selected configurations from the umbrella sampling windows close to the peak in the free energy profiles for each value of ε. For each selected configuration, we shoot 60 MD trajectories with randomized translational and rotational velocities of water molecules sampled from Maxwell−Boltzmann distribution. Committer value of a configuration is equal to the fraction of the MD trajectories that end up in the vapor basin. The configurations with committer values between 0.485 and 0.525 are considered to be part of the TSE. The graphs showing committer analysis for each value of ε are shown in Figure S1 and Figure S2 (Supporting Information).

Determining Radius of the Vapor Tube. The radius of the vapor tube in each configuration is estimated by employing a two-dimensional cluster analysis method. To understand this methodology, let us assume that the $x-y-z$ coordinate system is defined such that the two surfaces are parallel to the $y-z$ plane. We divide the $y-z$ plane in cells of dimension 0.2 × 0.2 Å^2. The centers of oxygen atoms of water molecules in the confined region are projected onto the $y-z$ plane. The cells whose centroids are within the distance of $\sigma_{\text{Oxygen}}/2 = 1.583$ Å from the center of any oxygen atom are labeled as "occupied", and the remaining cells are labeled as "vacant". Vacant cells which are adjacent to each other are considered as part of a single cluster. In this manner, all vacant cells are classified into different clusters. The largest cluster represents the vapor tube. Through this cluster analysis, only the vapor regions that span the entire distance from one surface to the other get included. A snapshot of a typical vapor tube is shown in Figure S3 (Supporting Information). Radius of the vapor tube is calculated from the area in the $y-z$ plane by assuming that the vapor tube is a cylinder. The error in the estimate of critical radius is determined from the standard deviation of critical radius values obtained from different configurations comprising the TSE.

2.3. Determination of Contact Angle and Line Tension for Different Surfaces.

We calculate the contact angle of water, θ and the solid−liquid−vapor line tension, λ for the surfaces of different ε. According to the modified Young equation, contact angle of a nanometer-sized droplet of liquid of radius r, θ_r is related to the macroscopic contact angle, θ by the following relation:[27,28]

$$\cos\theta_r = \cos\theta - \frac{\lambda}{R\gamma_{LV}} \tag{1}$$

Here λ is the line tension, R is the radius of the contact line ($R = r \sin\theta_r$), and Υ_{LV} is the liquid−vapor surface tension. We perform MD simulations of water droplets with the number of molecules ranging from 4000 to 30270 (corresponding to droplets of diameter ∼30 to 60 Å) on surfaces with different values of ε of the top two layers of atoms and a fixed ε of 0.0578 kcal/mol for the bottom layer. The surfaces span the entire $x-y$ plane of the simulation box, and comprise of three layers of atoms, similar in structure to those shown in Figure 1. The system is periodic in the $x-y$ directions. The dimensions of the simulation box is taken large enough that the droplets do not interact with their images. The simulations are initialized by placing a sphere-shaped water box containing the requisite number of water molecules on the surface. Canonical ensemble MD simulations at $T = 300$ K are performed. From the MD simulations, average contact angle from the last 2 ns is compared against the average contact angle from the previous 2 ns. If the contact angle is found to be invariant within the error bars then the system is assumed to have reached equilibrium. For the smallest droplets, 2 ns of equilibration time is found to be sufficient. While for the largest droplets, we perform 6 ns of equilibration simulations. Contact angle is calculated from 4 ns of production run after equilibration. To determine the shape of the droplet, we calculate the location of Gibbs dividing surface, r_{GDS} as a function of distance from the surface, z. If center of the droplet is at $r = 0$, the r_{GDS} is the radius where the following equation is satisfied,

$$\int_0^{r_{GDS}} (\rho_{liq,bulk} - \rho(r))\,\mathrm{d}r = \int_{r_{GDS}}^{\infty} \rho(r)\,\mathrm{d}r \tag{2}$$

An equation of circle is fitted to r_{GDS} as a function of z from which the contact angle, θ is calculated.[28] From the slope of the best-fit line to $\cos\theta_r$ and $1/R$, the value of λ/Υ_{LV} is estimated for each surface. To estimate the value of macroscopic contact angle, θ, we conduct MD simulations of a cylindrical droplet placed on the surfaces with different values of ε. To generate a cylindrical droplet, the dimension of one side of the simulation box (y-axis) is kept smaller than the x- and z-axis, so that the droplet interacts with its image to form an infinitely long cylindrical droplet.[28] For a droplet of radius r, the length of the y-axis should be less than $2\pi r$ to ensure that Plateau−Rayleigh instability is suppressed and a stable cylindrical droplet is formed.[28] The error in the measurement of contact angle is determined by using the method of block-averages in the simulations.[24] Figure S4 (Supporting Information) shows a snapshot of the equilibrated spherical and cylindrical droplets placed on a surface with $\varepsilon = 0.035$ kcal/mol. Figure S5 (Supporting Information) shows the graph of $\cos\theta_r$ versus $1/R$ for $\varepsilon = 0.025$ kcal/mol and $\varepsilon = 0.035$ kcal/mol. The error in line tension calculations are estimated by determining the maximum variation that is possible in the slope of the best-fit line of the graph of $\cos\theta_r$ versus $1/R$ when the error-bars in cos θ_r are included. It should be noted that another way of estimating the macroscopic contact angle is to extrapolate the spherical droplet results to $R \to \infty$. However, such a large extrapolation may lead to erroneous estimates. Hence, we prefer to calculate the macroscopic contact angle from simulating cylindrical droplets. For $\varepsilon = 0.035$ kcal/mol, for example, the contact angle from $R \to \infty$ extrapolation is found to be 120° while the simulation of a cylindrical droplet gives us a value of 116 ± 1.3°.

3. RESULTS AND DISCUSSION

3.1. Free Energy Profiles. Figure 3 shows free energy profiles of water confined between two hydrophobic surfaces as a function of the number of confined water molecules, N for different values of ε. $N \sim 270$ indicates the free energy basin of the liquid phase and $N \sim 10$ represents that of the vapor phase. The region around to the local maximum in the free energy profiles harbors the transition state between the liquid and the vapor phases. As expected, the relative stability of the vapor phase with respect to the liquid phase increases as the surfaces become more hydrophobic, that is, as ε decreases. For $\varepsilon > 0.04$ kcal/mol, the vapor phase is unstable. In the liquid basin, due to large density fluctuations, spontaneous formation and disappearance of vapor bubbles occurs.[9] The vapor bubbles may coalesce to form a region devoid of water molecules which spans from one hydrophobic surface to the other. Such a region is called a vapor tube. Vapor phase is nucleated and grows in the confined region when the vapor tube becomes larger than some critical size. Therefore, the liquid basin of the free energy profiles is characterized by formation of vapor bubbles and the vapor basin is characterized by the growth of a vapor tube. It is observed in Figure 3 that for small values of ε ($\varepsilon \leq 0.032$ kcal/mol), an abrupt change in the slope of the free energy profiles occurs close to $N \sim 205$, which represents a nondifferentiable point or a "kink". This kink in the profiles has been studied by Remsing et. al[20] and is a result of an abrupt transition from the free energy profiles associated with the formation of vapor bubbles to those associated with the formation of vapor tubes. As a result, the observed free energy barrier to evaporation in the presence of a kink is lower than predicted by classical nucleation theory.[20] For $\varepsilon = 0.035$ and 0.038 kcal/mol, the kink in the free energy profiles is less noticeable because the formation of the vapor tube at the kink is no longer the free energy barrier to evaporation. Instead, for these ε values, the vapor tube needs to grow further to achieve the critical size.

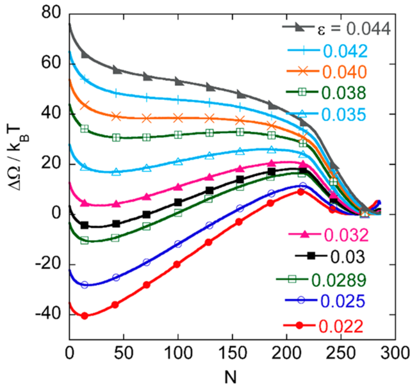

Figure 3. Free energy profiles of water confined between two hydrophobic surfaces of lateral size 30 × 30 Å^2 and separated by a distance of $D = 14$ Å, as a function of N. The LJ well-depth parameter for the interaction between surface atoms and water-oxygen, ε, for the inner two layers of atoms of the surfaces is varied from 0.022 to 0.044 kcal/mol.

3.2. Thermodynamic Relations. The goal of this work is to examine how good is the agreement between macroscopic thermodynamic theories in explaining the observed behavior of confined water. For this purpose, we present derivations of thermodynamic relations in this section.

Free Energy of Formation of Vapor Tubes. Thermodynamics of formation of vapor tubes has been discussed before.[11,16,18] In this section, we revisit the derivation to highlight some new points. The free energy of a confined liquid phase, Ω_L is given by

$$\Omega_L = 2L^2\gamma_{SL} - P_L L^2 D \tag{3}$$

where L is the lateral size of the surfaces, γ_{SL} is the solid−liquid surface tension, D is the confinement gap, and P_L is the pressure. Now, consider the state where the confined region harbors a cylindrical vapor tube of radius r. The free energy of this state is given by

$$\begin{aligned}\Omega_{tube} = {}& (2L^2 - 2\pi r^2)\gamma_{SL} + 2\pi r^2\gamma_{SV} - P_L(L^2D - \pi r^2 D) \\ & + 2\pi r D\gamma_{LV} - P_V\pi r^2 D + 4\pi r\lambda\end{aligned} \tag{4}$$

where γ_{SV} is the liquid−vapor surface tension, P_V is the vapor pressure, and λ is the solid−liquid−vapor line tension. The free energy change, $\Omega_{tube} - \Omega_L = \Delta\Omega$ is given by

$$\Delta\Omega = 2\pi r^2\gamma_{LV}\cos\theta + \pi r^2 D\Delta P + 2\pi r D\gamma_{LV} + 4\pi r\lambda \tag{5}$$

In the above equation, we have used Young's relation: $\gamma_{SV} - \gamma_{SL} = \gamma_{LV}\cos\theta$. ΔP is defined as $P_L - P_V$. The radius of the critical vapor tube, r^* can be found by setting $\frac{d\Delta\Omega}{dr} = 0$, which gives,

$$r^* = -\frac{D\gamma_{LV} + 2\lambda}{2\gamma_{LV}\cos\theta + D\Delta P} \tag{6}$$

By substituting (6) into (5), we get the free energy barrier associated with the formation of the critical vapor tube,

$$\Delta\Omega^* = \frac{-\pi(D\gamma_{LV} + 2\lambda)^2}{2\gamma_{LV}\cos\theta + D\Delta P} \tag{7}$$

In terms of r^*, the expression becomes

$$\Delta\Omega^* = -\pi r^{*2}(2\gamma_{LV}\cos\theta + D\Delta P) \tag{8}$$

For our system of interest, $\gamma_{LV} \sim O(10^{-2}\ \mathrm{N/m})$, $D \sim 1$ nm and $\Delta P \sim 1$ bar. Hence, $\gamma_{LV} \gg D\Delta P$. Neglecting the $D\Delta P$ term from eqs 6, 7, and 8, we get the following expressions:

$$r^* = \frac{-1}{\cos\theta}\left(\frac{D}{2} + \frac{\lambda}{\gamma_{LV}}\right) \tag{9}$$

$$\Delta\Omega^* = \frac{-2\pi\gamma_{LV}}{\cos\theta}\left(\frac{D}{2} + \frac{\lambda}{\gamma_{Lv}}\right)^2 \tag{10}$$

$$\Delta\Omega^* = -2\pi r^{*2}\gamma_{LV}\cos\theta \tag{11}$$

DOI: 10.1021/acs.jpcb.8b09026
J. Phys. Chem. B 2018, 122, 12087−12096

From eq 10, it is clear that $\Delta\Omega^*$ varies as D^2. An important new point that we want to highlight is that the role of line tension is more subtle than what has been previously discussed.[16] The line tension term enters eq 10 as an adjustment to the actual confinement gap, D. According to macroscopic theory, the free energy barrier to evaporation scales as $\left(\frac{D}{2} + \frac{\lambda}{\gamma_{Lv}}\right)^2$. The ratio λ/γ_{LV} is of the order of molecular length-scales[29,30] and therefore when the confinement gap, D is of the order of nanometers, the inclusion of line-tension term in macroscopic theory is expected to be important. Radius of the critical vapor tube scales by $\left(\frac{D}{2} + \frac{\lambda}{\gamma_{Lv}}\right)$ and again the line-tension term is expected to be important at nanoscale confinement. Equation 11 shows that the $\Delta\Omega^*$varies as r^{*2}. It is easily verified that the expression in eq 11 is invariant of whether line-tension is included in the free energy expression or not.

Free Energy of Condensation of Water in the Confined Region. Following a similar procedure as above, the free energy barrier associated with the condensation of water in the confined region can be derived as well. The free energy of the vapor phase is given by

$$\Omega_V = 2L^2\gamma_{LV} + 4LD\gamma_{LV} - P_V L^2 D + 8L\lambda \tag{12}$$

Subtracting eq 4 and using Young's relation we get,

$$\begin{aligned}\Delta\Omega_V &= 2(\pi r^2 - L^2)\gamma_{LV}\cos\theta + (\pi r^2 - L^2)D\Delta P \\ &\quad + 2(\pi r - 2L)D\gamma_{LV} + 4(\pi r - 2L)\lambda\end{aligned} \tag{13}$$

By setting $\frac{\mathrm{d}\Delta\Omega_V}{\mathrm{d}r} = 0$, we obtain the same expression for r^* as in eq 6, which is substituted back to eq 13 to get the free energy barrier to condensation of water in the confined region, $\Delta\Omega_V^*$.

Free Energy of Formation of Vapor Bubbles on Hydrophobic Surfaces. In the liquid phase, vapor bubbles form on the hydrophobic surfaces which eventually coalesce to form a vapor tube. Hence, the free energy profile of confined water in the liquid basin can be modeled as the free energy of formation of vapor bubbles.[31] It is assumed that vapor bubbles form on both surfaces, and that the vapor−liquid interface of these bubbles attains equilibrium contact angle. Under these assumptions, the free energy of forming a vapor bubble on both surfaces is given by[31]

$$\begin{aligned}\Omega_{bubble} &= -2P_V V_b + 2\pi r_b^{\,2}\gamma_{SV} + 2A_b\gamma_{LV} + 4\pi r_b\lambda \\ &\quad - (L^2 D - 2V_b)P_L + 2(L^2 - \pi r_b^{\,2})\gamma_{SL}\end{aligned} \tag{14}$$

Here, r_b is the radius and V_b is the volume of the bubble. A_b is the area of the liquid−vapor interface of the bubble. The following relations can be derived by assuming the bubble to be part of a sphere,

$r_b = \left(\frac{3V_b\phi}{\pi}\right)^{1/3}$ where $\phi = \frac{\sin\theta(1-\cos\theta)}{(2-\cos\theta)(1+\cos\theta)}$, and $A_b = \pi(r_b^{\,2} + h^2)$ where h is the height of the bubble, given by $h = r_b\frac{1+\cos\theta}{\sin\theta}$.The expression for change in free energy is obtained by subtracting eq 3 from eq 14,

$$\Delta\Omega_{bubble} = 2\pi\gamma_{LV}\left(r_b^{\,2}(1+\cos\theta) + h^2 + 2r_b\frac{\lambda}{\gamma_{LV}}\right) \tag{15}$$

In the above equation, we have ignored the ΔP term as before.

3.3. Comparison between Theory and Simulation Results.

For comparing the predictions from the above-derived equations with the results from molecular simulations, we have estimated the following quantities: r^* (critical radius of vapor tube), λ (line tension), and θ (contact angle) using the methodologies described in the Simulations System and Methods. Table 1 lists the values of these quantities for different ε. The ratio of line-tension to surface tension, λ/Υ_{LV} is of molecular size and negative in agreement with previous works.[30,32] In Figure 4, the free energy barrier to evaporation, $\Delta\Omega^*$ is plotted as a function of ($-r^{*2}\cos\theta$). From eq 11 one can see that the slope of this graph is equal to $2\pi\,\Upsilon_{LV}$. From the best fit line, the Υ_{LV} is estimated to be 0.043 N/m. This value deviates from the bulk surface tension of SPC/E water (0.063 N/m).[33] However, the deviation is not particularly surprising because liquid water confined in nanometer-sized region is arranged in layers. Such an arrangement is quite distinct from the bulk structure and hence water may not retain bulk properties.[34] This mismatch may also be due to the inadequacy of macroscopic theory. Nevertheless, we will show in this work that with this value of Υ_{LV}, the macroscopic theory is quite consistent with the simulation results.

Table 1. Different Thermodynamic Properties of the System Estimated from Simulations[a]

ε (kcal/mol)	λ/Υ_{LV} (Å)	θ (deg)	r^* (Å)
0.022	−3.6 (0.27)	131 (1.5)	5.2 (0.08)
0.025	−3.4 (0.17)	128 (2.2)	5.5 (0.46)
0.0289	−3.3 (0.33)	123 (2.0)	6.7 (0.50)
0.03	−3.1 (0.32)	122 (2.0)	7.3 (0.64)
0.032	−2.8 (0.19)	120 (1.3)	7.9 (0.57)
0.035	−2.4 (0.32)	116 (1.3)	9.1 (0.48)
0.038	−2.2 (0.04)	113 (1.2)	10.6 (0.50)
0.04	−2.1 (0.61)	111 (0.6)	12.5 (0.25)

[a] The values in parentheses represent errors in the estimation.

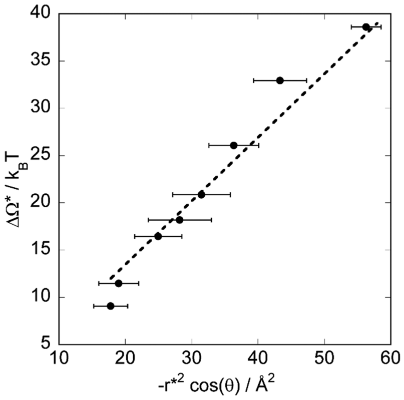

Figure 4. Free energy barrier to evaporation of water in the confined region, $\Delta\Omega^*$ as a function of $(-r^{*2}\cos(\theta))$ where r^* is the radius of the critical vapor tube. From eq 11, the slope of the best fit line is equal to $2\pi\gamma_{LV}$ where γ_{LV} is the liquid−vapor surface tension.

Using eq 10, $\Delta\Omega^*$ can be estimated from macroscopic theory. Figure 5a shows a comparison of $\Delta\Omega^*$ obtained from molecular simulations and the one estimated from eq 10 as a function of ε. It is observed that for the conditions where the vapor phase is more stable than the liquid phase ($\varepsilon \leq 0.032$

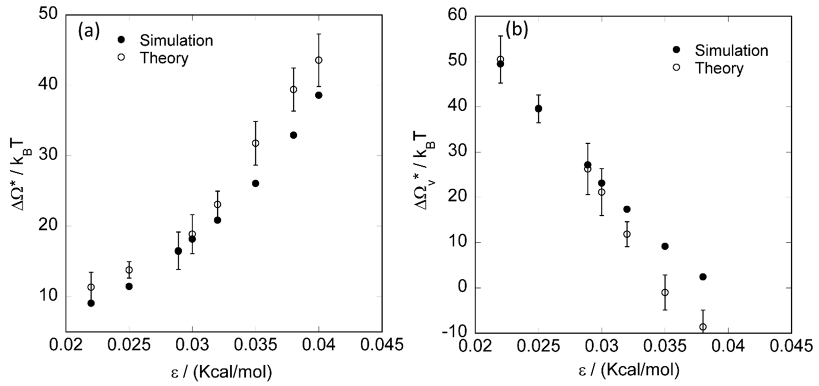

Figure 5. Comparison of (a) free energy barrier to evaporation of water, $\Delta\Omega^*$ and (b) free energy barrier to condensation of water, $\Delta\Omega^*_V$ in the confined region as a function of ε with predictions from macroscopic theory (eq 10 and eq 13 respectively). It is observed that both $\Delta\Omega^*$ and $\Delta\Omega^*_V$ are predicted well by macroscopic theory for small values of ε ($\leq$0.032 kcal/mol).

kcal/mol), the estimates from macroscopic theory are in very good agreement with the results of molecular simulations. For $\varepsilon \leq 0.032$ kcal/mol, the theoretical predictions of $\Delta\Omega^*$ are slightly higher than those from simulations. This is expected as the presence of a kink in the free energy profiles lowers the observed free energy barrier.[20] For $\varepsilon > 0.032$ kcal/mol, the theory overpredicts the $\Delta\Omega^*$ by ~5 k_BT. Overall, macroscopic theory is found to be sufficiently good in matching the simulation results for $\Delta\Omega^*$. Figure 5b compares the $\Delta\Omega^*_V$ obtained from molecular simulations and the one estimated from eq 13 as a function of ε. It is observed that for $\varepsilon \leq 0.032$ kcal/mol, the estimates from macroscopic theory are in very good agreement with the results of molecular simulations. For $\varepsilon > 0.032$ kcal/moI, the theory under-predicts the $\Delta\Omega^*_V$. In Figure 6, the r^* predicted from macroscopic theory eq 9 is compared against the results from molecular simulations. The theoretical estimates match well with the results of molecular simulations apart from some deviation observed at larger values of ε. From Figure 5 and Figure 6, it is concluded that macroscopic theory is sufficiently good in quantitatively predicting the free energy barrier and the size of the critical vapor tube. Some deviations between macroscopic theory and molecular simulation results are observed for larger values of ε. At this point, one can conjecture as to why the theoretical predictions deviate at larger values of ε. For $\varepsilon \geq 0.035$ kcal/mol, the r^* becomes as large as 9−12.5 Å. The diameters of these vapor tubes are comparable to the lateral dimensions of the surfaces, $L \sim 30$ Å. Hence, there may be some unaccounted edge effects that are responsible for the observed divergence. To verify this conjecture, one would need to perform the same analysis for larger surfaces. However, the computational cost of simulating a bigger system is quite large. As previous works have shown,[13,20] the vapor tubes that form in the confined region are not cylindrical but fluctuate in many different shapes. Hence, macroscopic theory developed for a vapor tube with a fixed geometry and size is only an approximation. Nevertheless, predictions from macroscopic theory are found to be sufficiently good in matching simulation results.

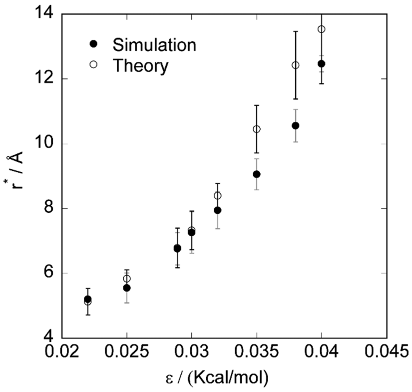

Figure 6. Comparison of radius of the critical vapor tube, r^* from simulations with prediction from macroscopic theory eq 9 as a function of ε. The theoretical predictions match the simulation results reasonably well.

In the above analysis, the confinement gap D has been kept fixed at 14 Å while the interaction of the surface atoms with water-oxygen is varied. This allows us to systematically investigate the role of thermodynamic properties, such as line tension and contact angle on the behavior of water under confinement. In Figure 7, the $\Delta\Omega^*$ from molecular simulations, obtained for fixed surface properties but changing D, is compared against predictions from macroscopic theory eq

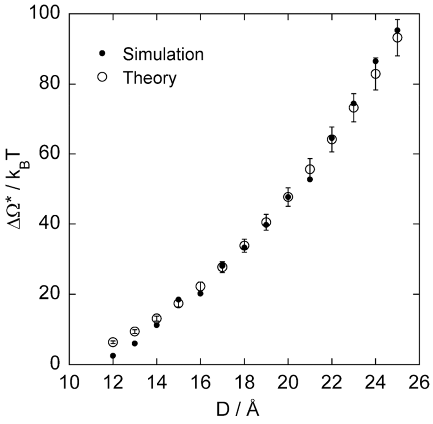

Figure 7. Comparison between free energy barriers to evaporation, $\Delta\Omega^*$ obtained from molecular simulations (data from Remsing et. al) and theoretical prediction from eq 10 as a function of confinement gap, D. For the theoretical fit, our estimated values of $\Upsilon_{LV} = 0.043$ N/m and a contact angle, θ of 123 ± 2° is used. The best fit of eq 10 is obtained for a value of $\lambda/\Upsilon_{LV} = -3.7$ Å, which is close to our estimated value of -3.3 ± 0.33 Å. A very good match between simulation results and theoretical predictions is observed.

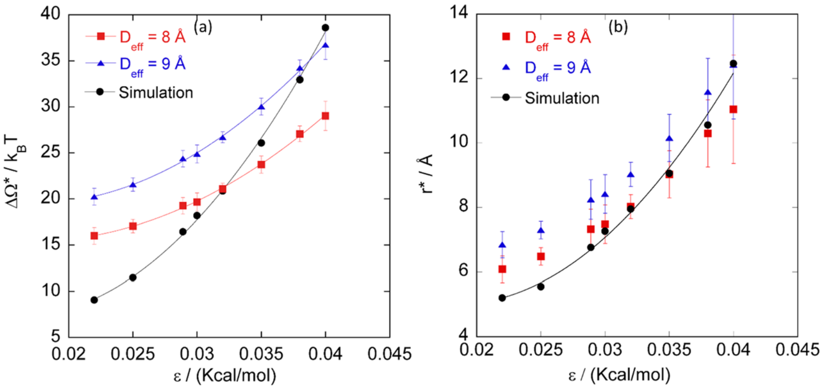

Figure 8. Comparison between theoretical predictions and simulation results when the role of line tension is omitted. (a) shows the free energy barrier to evaporation, ΔΩ*, and (b) shows the critical radius, r^* plotted as a function of ε from simulations and predicted from eq 10 and eq 9, respectively, by ignoring the line tension term and for two different values of effective confinement gap, D_{eff} = 8 and 9 Å. A mismatch in the trends of ΔΩ* and r^* from macroscopic theory without the line tension term and the simulation results is observed. Lines in the graphs are a guide to the eye.

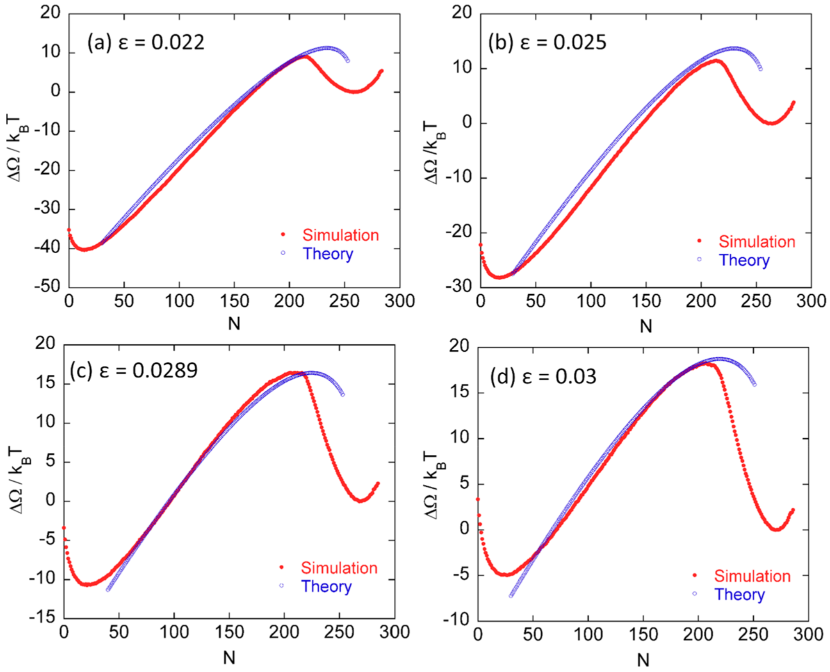

Figure 9. Free energy profiles obtained from simulations are compared to predictions from macroscopic theory for the branch of the profile harboring a vapor tube eq 5 for different values of ε. A very good match between simulations and theoretical predictions is observed for these values of ε. The error bars in the theoretical predictions are of the order of 2−5 k_BT (same as shown in Figure 5). The error-bars are not shown explicitly to unclutter the graph.

10. The simulations data in Figure 7 is from Remsing et al.[20] (Figure S8) in the Supporting Information. In the study by Remsing et al., the free energy profiles of water confined between two square surfaces of lateral dimensions, $L \sim 40$ Å were determined.[20] Similar to our system, their surfaces comprised of LJ atoms arranged in a hexagonal lattice with a lattice constant of 1.4 Å. The value of the ε parameter of the LJ interactions between a surface atom and water-oxygen was chosen as 0.0289 kcal/mol.[20] For comparing the simulation results in Figure 7 with theoretical predictions, eq 10 is employed with the values of Υ_{LV} and θ corresponding to ε = 0.0289 kcal/mol taken from Table 1. The ratio $\lambda/\ \Upsilon_{LV}$ is used as the best-fit parameter for the simulations data. The best fit value of $\lambda/\ \gamma_{LV}$ is found to be −3.7 Å, which is not far from our calculated value of −3.3 ± 0.33 Å. A very good fit between simulations and theory is found in Figure 7, indicating that macroscopic theory is quantitatively correct in predicting simulation results.

Importance of Line-Tension in Macroscopic Theory. The derivations of thermodynamic relations discussed in the section above include the effect of line-tension. In previous works, the role of line-tension has been ignored.[12,18] In our derivation of eq 10, we show that line-tension acts to decrease the effective confinement gap in the expression of free energy barrier to evaporation. Hence, the role of line-tension is expected to be important when the confinement gap is of the order of a few nanometers. Previous investigators have shown that the free energy barrier is proportional to $D_{eff}{}^2 = (D - 2l)^2$ where l is the mean vapor film thickness.[18] From our simulations, the average vapor film thickness is ~2.5 Å, so

DOI: 10.1021/acs.jpcb.8b09026
J. Phys. Chem. B 2018, 122, 12087−12096

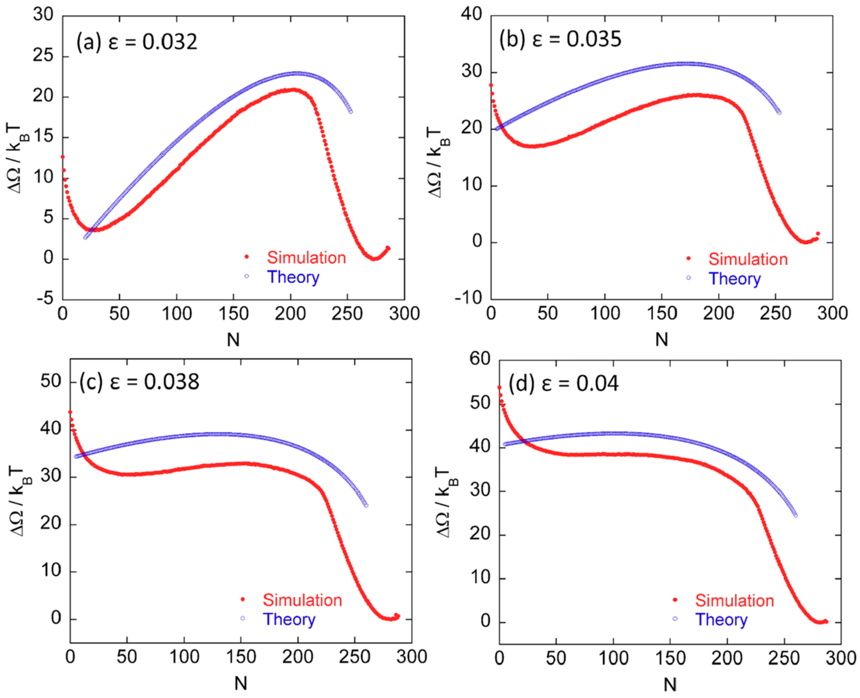

Figure 10. Free energy profiles obtained from simulations are compared to predictions from macroscopic theory for the branch of the profile harboring a vapor tube eq 5 for different values of ε. The free energy profiles from theoretical predictions are found to systematically deviate in comparison to the simulations. This deviation is equal to the overprediction of $\Delta\Omega^*$ observed in Figure 5. Apart from this shift, the predicted free energy profiles capture the overall shape of the profiles from simulations very well. The error bars in the theoretical predictions are of the order of 2−5 k_BT (same as shown in Figure 5). The error-bars are not shown explicitly to unclutter the graph.

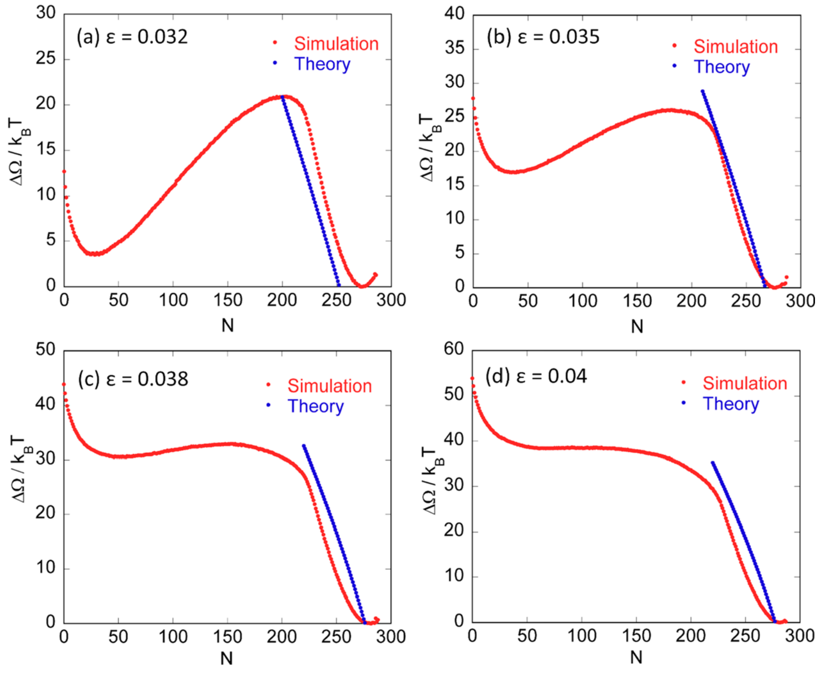

Figure 11. Free energy profiles obtained from simulations are compared to predictions from macroscopic theory for the branch of the profile harboring vapor bubbles eq 15 for different values of ε. The free energy profiles from theoretical predictions deviate in comparison to the simulations. The predicted free energy profiles capture the overall shape of the profiles from simulations well. The error bars in the theoretical predictions are of the order of 2−5 k_BT (same as shown in Figure 5). The error-bars are not shown explicitly to unclutter the graph.

that $D_{eff} \sim 9$ Å. However, by taking $\lambda = 0$ in the macroscopic theory eq 10, the best-fit to $\Delta\Omega^*$ is found for $D_{eff} = 8$ Å. Figure 8a compares theoretical predictions of $\Delta\Omega^*$ by taking $D_{eff} = 8$ and 9 Å with the results from simulations. It is observed that macroscopic theory with $\lambda = 0$ is unable to capture the correct trend of $\Delta\Omega^*$. That is, the slope of $\Delta\Omega^*$ versus ε predicted from theory when $\lambda = 0$ is different from that obtained from the simulations. Figure 8b compares the prediction of r^* from eq 9 with $\lambda = 0$ and the results from the simulations. A deviation between the trends is again observed. Therefore, it is concluded that inclusion of line tension in macroscopic theory is important for correctly capturing the behavior of water under hydrophobic confinement. Lefevre et al.[32] found that the inclusion of line-tension is necessary to account for their experimentally observed values of nucleation barriers associated with the extrusion of water from hydrophobic mesopores. Hence, our conclusions on the importance of line-tension are supported by experimental results.

Quantitative Accuracy of Macroscopic Theory in Predicting Free Energy Profiles. Next, we analyze how good is macroscopic theory in predicting the free energy profiles of water under hydrophobic confinement. Equation 5 is the equation for the change in free energy, $\Delta\Omega$, as a function of the size of the vapor tube, r. In Figure 9a–d, a comparison of free energy profiles in the vapor basin predicted from eq 5 and obtained from molecular simulations is shown for different $\varepsilon \leq 0.03$ kcal/mol. In eq 5, the radius of the vapor tube is calculated as $r = \left(\frac{N_{liq} - N}{\pi N_{liq}}\right)^{0.5} L$. It is observed that macroscopic theory is quantitatively correct in predicting the free energy profiles in the vapor basin for $\varepsilon \leq 0.03$ kcal/mol. Figure 10a–d show a similar comparison for $\varepsilon \geq 0.032$ kcal/mol. It is observed that the free energy profiles predicted from eq 5 systematically deviate by a constant value from those obtained from simulations. It is noted, however, that the slope of the free energy profiles from eq 5 and from molecular simulations match well for all values of ε. Therefore, a qualitative match is achieved for $\varepsilon \geq 0.032$ kcal/mol.

Finally, we analyze how good is macroscopic theory of free energy profiles of formation for vapor bubbles eq 15 by comparing the predictions to molecular simulation results. In eq 15, the volume of the vapor bubble is calculated as $V_b = \left(\frac{N_{liq} - N}{2N_{liq}}\right) L^2 D_{eff}$ where N_{liq} is the number of confined water molecules corresponding to the minimum in the liquid basin, N is the number of confined water molecules in the configuration and D_{eff} is the effective confinement gap. For this calculation, $D_{eff} = 9$ Å.

Figure 11a–d shows a comparison of predictions from eq 15 with the free energy profiles from simulations for $\varepsilon \geq 0.032$ kcal/mol. It is observed that the predictions from macroscopic theory qualitatively match the simulation results. The theoretical free energy profiles deviate from the experimental ones, but the slopes of the profiles match with the simulations. For $\varepsilon \leq 0.03$, however, the macroscopic theory of vapor bubble formation fails to match the simulation results (Figure S6 (Supporting Information)). We do not understand why theoretical predictions do not match the simulation results for small values of ε. One conjecture is that for more hydrophobic surfaces, on average, more than one vapor bubble nucleates on the surfaces.

4. CONCLUSIONS

We have determined the free energy profiles of water confined between surfaces of varying hydrophobicity using indirect umbrella sampling (INDUS) technique in molecular dynamics simulations. We have also performed independent simulations to estimate contact angle, line tension and size of the critical vapor tube for these surfaces. From the simulation results and macroscopic theory, we have estimated the value of liquid–vapor surface tension of confined water. By comparing the predictions of macroscopic theory and simulation results, we assert that the inclusion of line-tension is important in order to capture correct simulation trends. The free energy barrier to evaporation is found to scale by a factor of $(D/2 + \lambda/\Upsilon_{\mathrm{LV}})^2$, where D is the confinement gap and λ/Υ_{LV} is the ratio of line-tension and liquid–vapor surface tension. The radius of the critical vapor tube necessary for nucleating evaporation scales by a factor of $(D/2 + \lambda/\Upsilon_{\mathrm{LV}})$. We show that if the contribution of line tension is ignored then the macroscopic theory fails to match the simulation trends even in a qualitative manner. Macroscopic theory also quantitatively predicts the free energy profiles of the branch which harbors a vapor tube for systems wherein the vapor phase is the most stable phase. A qualitative match is observed between the free energy profiles predicted from macroscopic theory and those found from simulations for conditions wherein liquid water is more stable.

■ ASSOCIATED CONTENT

Ⓢ Supporting Information

The Supporting Information is available free of charge on the ACS Publications website at DOI: 10.1021/acs.jpcb.8b09026.

> Figure S1, committer values of different configurations as a function of radius of the vapor tube for ε ranging from 0.022 to 0.03 kcal/mol; Figure S2, committer values of different configurations as a function of radius of the vapor tube for ε ranging from 0.032 to 0.04 kcal/mol; Figure S3, snapshot of a vapor tube in the confined region observed by 2D projection of coordinates of confined water molecules on the y–z plane (plane parallel to the surfaces); Figure S4, snapshot of spherical and cylindrical droplets placed on the hydrophobic surface with $\varepsilon = 0.035$ kcal/mol for the determination of contact angle; Figure S5, graph of contact angle, $\cos\theta_r$, as a function of $1/R$, where R is the radius of a spherical droplet for (a) $\varepsilon = 0.025$ kcal/mol and (b) $\varepsilon = 0.035$ kcal/mol; Figure S6, free energy profiles obtained from simulations compared to the predictions from macroscopic theory for the branch of the profile harboring vapor bubbles for ε ranging from 0.022 to 0.03 kcal/mol (PDF)

■ AUTHOR INFORMATION

Corresponding Author

*(S.S.) E-mail: sharmas@ohio.edu.

ORCID

Sumit Sharma: 0000-0003-3138-5487

Notes

The authors declare no competing financial interest.

■ ACKNOWLEDGMENTS

Acknowledgement is made to the donors of the Petroleum Research Fund (ACS PRF number: 56892-DNI6), administered by the American Chemical Society, for support of this research. This work is supported by NSF CBET Grant 1705817. The authors thank Dr. Amish Patel for providing LAMMPS implementation of the INDUS code. Computational resources for this work were provided by the Ohio Supercomputer Center.

■ REFERENCES

(1) Barelier, S.; Boyce, S. E.; Fish, I.; Fischer, M.; Goodin, D. B.; Shoichet, B. K. Roles for Ordered and Bulk Solvent in Ligand

Recognition and Docking in Two Related Cavities. *PLoS One* **2013**, *8* (7), No. e69153.

(2) Wang, L.; Berne, B. J.; Friesner, R. A. Ligand Binding to Protein-Binding Pockets with Wet and Dry Regions. *Proc. Natl. Acad. Sci. U. S. A.* **2011**, *108* (4), 1326−1330.

(3) Zhou, R.; Huang, X.; Margulis, C. J.; Berne, B. J. Hydrophobic Collapse in Multidomain Protein Folding. *Science* **2004**, *305* (5690), 1605−1609.

(4) Kauzmann, W. Some Factors in the Interpretation of Protein Denaturation. *Adv. Protein Chem.* **1959**, *14*, 1−63.

(5) Rose, G. D.; Roy, S. Hydrophobic Basis of Packing in Globular-Proteins. *Proc. Natl. Acad. Sci. U. S. A.* **1980**, *77* (8), 4643−4647.

(6) Tanford, C. The Hydrophobic Effect and the Organization of Living Matter. *Science* **1978**, *200* (4345), 1012−1018.

(7) Tanford, C. *The Hydrophobic Effect: Formation of Micelles and Biological Membranes*, 2nd ed.; J. Wiley: 1980.

(8) Zhu, F.; Hummer, G. Pore Opening and Closing of a Pentameric Ligand-Gated Ion Channel. *Proc. Natl. Acad. Sci. U. S. A.* **2010**, *107* (46), 19814−19819.

(9) Patel, A. J.; Varilly, P.; Chandler, D. Fluctuations of Water near Extended Hydrophobic and Hydrophilic Surfaces. *J. Phys. Chem. B* **2010**, *114* (4), 1632−1637.

(10) Lum, K.; Chandler, D.; Weeks, J. D. Hydrophobicity at Small and Large Length Scales. *J. Phys. Chem. B* **1999**, *103* (22), 4570−4577.

(11) Cerdeirina, C. A.; Debenedetti, P. G.; Rossky, P. J.; Giovambattista, N. Evaporation Length Scales of Confined Water and Some Common Organic Liquids. *J. Phys. Chem. Lett.* **2011**, *2* (9), 1000−1003.

(12) Leung, K.; Luzar, A. Dynamics of Capillary Evaporation. II. Free Energy Barriers. *J. Chem. Phys.* **2000**, *113* (14), 5845−5852.

(13) Sharma, S.; Debenedetti, P. G. Free Energy Barriers to Evaporation of Water in Hydrophobic Confinement. *J. Phys. Chem. B* **2012**, *116* (44), 13282−13289.

(14) Zhang, Z.; Ha, M. Y.; Jang, J. Contrasting Water Adhesion Strengths of Hydrophobic Surfaces Engraved with Hierarchical Grooves: Lotus Leaf and Rose Petal Effects. *Nanoscale* **2017**, *9* (42), 16200−16204.

(15) Kim, H.; Saha, J. K.; Jang, J. Drying Transition of Water Confined between Hydrophobic Pillars. *J. Phys. Chem. C* **2012**, *116* (36), 19233−19239.

(16) Sharma, S.; Debenedetti, P. G. Evaporation Rate of Water in Hydrophobic Confinement. *Proc. Natl. Acad. Sci. U. S. A.* **2012**, *109* (12), 4365−4370.

(17) Lum, K.; Luzar, A. Pathway to Surface-Induced Phase Transition of a Confined Fluid. *Phys. Rev. E: Stat. Phys., Plasmas, Fluids, Relat. Interdiscip. Top.* **1997**, *56* (6), R6283−R6286.

(18) Luzar, A. Activation Barrier Scaling for the Spontaneous Evaporation of Confined Water. *J. Phys. Chem. B* **2004**, *108* (51), 19859−19866.

(19) Altabet, Y. E.; Debenedetti, P. G. The Role of Material Flexibility on the Drying Transition of Water between Hydrophobic Objects: A Thermodynamic Analysis. *J. Chem. Phys.* **2014**, *141* (18), 18C531.

(20) Remsing, R. C.; Xi, E.; Vembanur, S.; Sharma, S.; Debenedetti, P. G.; Garde, S.; Patel, A. J. Pathways to Dewetting in Hydrophobic Confinement. *Proc. Natl. Acad. Sci. U. S. A.* **2015**, *112*, 8181.

(21) Giovambattista, N.; Almeida, A. B.; Alencar, A. M.; Buldyrev, S. V. Validation of Capillarity Theory at the Nanometer Scale by Atomistic Computer Simulations of Water Droplets and Bridges in Contact with Hydrophobic and Hydrophilic Surfaces. *J. Phys. Chem. C* **2016**, *120* (3), 1597−1608.

(22) Almeida, A. B.; Giovambattista, N.; Buldyrev, S. V.; Alencar, A. M. Validation of Capillarity Theory at the Nanometer Scale. II: Stability and Rupture of Water Capillary Bridges in Contact with Hydrophobic and Hydrophilic Surfaces. *J. Phys. J. Phys. Chem. C* **2018**, *122* (3), 1556−1569.

(23) Berendsen, H. J. C.; Grigera, J. R.; Straatsma, T. P. The Missing Term in Effective Pair Potentials. *J. Phys. Chem.* **1987**, *91* (24), 6269−6271.

(24) Allen, M. P.; Tildesley, D. J. *Computer Simulation of Liquids*. Oxford University Press: 1989.

(25) Patel, A. J.; Varilly, P.; Chandler, D.; Garde, S. Quantifying Density Fluctuations in Volumes of all Shapes and Sizes using Indirect Umbrella Sampling. *J. Stat. Phys.* **2011**, *145* (2), 265−275.

(26) Kumar, S.; Rosenberg, J. M.; Bouzida, D.; Swendsen, R. H.; Kollman, P. A. The Weighted Histogram Analysis Method for Free-Energy Calculations on Biomolecules. I. The Method. *J. Comput. Chem.* **1992**, *13* (8), 1011−1021.

(27) Bresme, F.; Quirke, N. Computer Simulation Study of the Wetting Behavior and Line Tensions of Nanometer Size Particulates at a Liquid-Vapor Interface. *Phys. Rev. Lett.* **1998**, *80* (17), 3791.

(28) Weijs, J. H.; Marchand, A.; Andreotti, B.; Lohse, D.; Snoeijer, J. H. Origin of Line Tension for a Lennard-Jones Nanodroplet. *Phys. Fluids* **2011**, *23* (2), No. 022001.

(29) Amirfazli, A.; Neumann, A. W. Status of the Three-Phase Line Tension: A Review. *Adv. Colloid Interface Sci.* **2004**, *110* (3), 121−141.

(30) Berg, J. K.; Weber, C. M.; Riegler, H. Impact of Negative Line Tension on the Shape of Nanometer-Size Sessile Droplets. *Phys. Rev. Lett.* **2010**, *105* (7), No. 076103.

(31) Jabes, B. S.; Driskill, J.; Vanzo, D.; Bratko, D.; Luzar, A. Metastable Vapor in a Janus Nanoconfinement. *J. Phys. Chem. C* **2017**, *121* (24), 13144−13150.

(32) Lefevre, B.; Saugey, A.; Barrat, J.-L.; Bocquet, L.; Charlaix, E.; Gobin, P.-F.; Vigier, G. Intrusion and Extrusion of Water in Hydrophobic Mesopores. *J. Chem. Phys.* **2004**, *120* (10), 4927−4938.

(33) Vega, C.; De Miguel, E. Surface Tension of the Most Popular Models of Water by using the Test-Area Simulation Method. *J. Chem. Phys.* **2007**, *126* (15), 154707.

(34) Leong, K.-Y.; Wang, F. A Molecular Dynamics Investigation of the Surface Tension of Water Nanodroplets and a New Technique for Local Pressure Determination through Density Correlation. *J. Chem. Phys.* **2018**, *148* (14), 144503.